

FuseFormer: A Transformer for Visual and Thermal Image Fusion

Aytekin Erdogan, Erdem Akagündüz
Department of Modeling and Simulation
Graduate School of Informatics
Middle East Technical University, Ankara, Türkiye
{aytekin.erdogan, akaerdem}@metu.edu.tr

Abstract—Due to the lack of a definitive ground truth for the image fusion problem, the loss functions are structured based on evaluation metrics, such as the structural similarity index measure (SSIM). However, in doing so, a bias is introduced toward the SSIM and, consequently, the input visual band image. The objective of this study is to propose a novel methodology for the image fusion problem that mitigates the limitations associated with using classical evaluation metrics as loss functions. Our approach integrates a transformer-based multi-scale fusion strategy that adeptly addresses local and global context information. This integration not only refines the individual components of the image fusion process but also significantly enhances the overall efficacy of the method. Our proposed method follows a two-stage training approach, where an auto-encoder is initially trained to extract deep features at multiple scales in the first stage. For the second stage, we integrate our fusion block and change the loss function as mentioned. The multi-scale features are fused using a combination of Convolutional Neural Networks (CNNs) and Transformers. The CNNs are utilized to capture local features, while the Transformer handles the integration of general context features. Through extensive experiments on various benchmark datasets, our proposed method, along with the novel loss function definition, demonstrates superior performance compared to other competitive fusion algorithms.

Index Terms—RGB-T Image Fusion, Vision Transformers, Structural Similarity Metric

I. INTRODUCTION

Image fusion is a powerful technique in the context of computer vision that involves combining information from multiple images taken at different wavelengths or bands to create a single, unified representation. The primary objective of image fusion is to extract and integrate complementary details and features from each input image, resulting in a more informative and enhanced composite image. The fusion of images from different bands is widely used in various applications, such as night vision [1] and thermal imaging [2], remote sensing [3] and multi-modal medical imaging [4], just to name a few.

Research on image fusion dates back decades, with [5] being one of the pioneering studies. Traditional image fusion algorithms—that is, those prior to deep learning—have been thoroughly studied in the literature [6]. A significant concern with these methods lies in the incorporation of handcrafted steps, leading to suboptimal outcomes for changing conditions. With the deep learning (DL) era, attempts have been made to address this issue using Convolutional Neural Networks



(a) Visual band (b) Thermal band (c) FuseFormer

Fig. 1: Example output from the proposed FuseFormer model: Fusion of visual and thermal images.”

(CNNs) [7]–[10], autoencoders [11], [12], attention models [13], and Generative Adversarial Networks (GANs) [14]–[21]. These first-generation of DL approaches are significantly better than the pre-DL era methods, but still exhibit limitations in effectively capturing long-range dependencies (i.e. global context) within the image. To address this challenge, Vision Transformers [22], [23] have been utilized for image fusion tasks [24]–[30].

Despite these significant advancements, a notable gap is apparent in the literature: the reliance on evaluation metrics such as the Structural Similarity Index (SSIM) [31] as the primary component of the loss function. While this approach may produce satisfactory quantitative results, it may provide nonoptimal results [32]. Our contributions to this issue, as well as other aspects of our work, can be summarized as follows:

- We propose a novel fusion framework, called the FuseFormer, that utilizes a Transformer+CNN fusion block with a unique loss function that takes both modalities into account. By doing so, it mitigates the gap between quantitative and qualitative results.
- The proposed method utilizes Transformers to capture global context and combines the results with local features obtained from Convolutional Neural Networks (CNNs).
- The proposed method is evaluated on multiple fusion benchmark datasets, where we achieve competitive results compared to existing fusion methods.

II. RELATED WORK

As briefly introduced in the previous section, in the last four decades of research, the RGB and infrared image fusion

domain has been the subject of extensive research, spanning from traditional fusion algorithms [6] to state-of-the-art Transformer-based models [33]–[37]. Traditional algorithms, relying on handcrafted steps, faced challenges in adaptability and time complexity [33]–[37]. The scarcity of labeled datasets for RGB-IR fusion prompted a shift towards unsupervised scenarios [38], which also guided our investigation towards enhancing evaluation metrics in this paper.

With the advent of deep learning, learning-based algorithms became predominant, categorized by learning methods, loss functions, and the use of labeled datasets [8], [9], [14], [39]. CNN-based approaches, both supervised and unsupervised, exhibited success in feature extraction for image fusion, yet challenges persisted in scenarios with significant changes in factors like illumination or resolution [39]. Autoencoder-based algorithms, utilizing neural networks for dimensionality reduction, showcased advancements in works such as [11], [12].

GAN-based methods focused on unsupervised fusion, integrating attention mechanisms and residual connections for improved performance [14], [19], [40]. While these approaches demonstrated promise, challenges persisted in effectively handling the inherent differences between fused and source images.

A literally “transformative” shift in RGB-IR image fusion occurred with the introduction of Vision Transformer-based algorithms in 2021 [22]–[24]. These methodologies, driven by the self-attention mechanism, marked a paradigm shift by efficiently managing long-range dependencies in images. Innovative designs, such as multiscale fusion strategies and dual transformer approaches, were introduced, emphasizing the seamless integration of Transformers with traditional methods [25], [26], [29], [41]. Unsupervised Transformer-based techniques, reliant on loss functions, eliminated the need for labeled data but posed challenges in methodological evaluations [25], [29]. Ongoing research explores diverse Transformer integrations, Transformer-CNN combinations, and the utilization of auxiliary information to further enrich the fusion process [25], [26], [29], [41]. The integration of deep learning methods has not only enhanced feature extraction capabilities but has also paved the way for more adaptive and robust solutions in the challenging methodologies of image fusion. For a comprehensive overview, readers are directed to Zhang et al. [42] which provides insights into the broader landscape of RGB-IR image fusion research, including advancements, methodologies, and challenges. For a review of RGB-IR image and videos set, which serves as the application data for fusion algorithms, readers may refer to [43].

III. METHODOLOGY

In general terms, the image fusion operation can be decomposed into three key components: the feature extractor, feature fuser, and the image reconstructor. Although these components may differ from architecture to architecture, it is possible to define their purposes such that the feature extractor is responsible for extracting multilevel features from

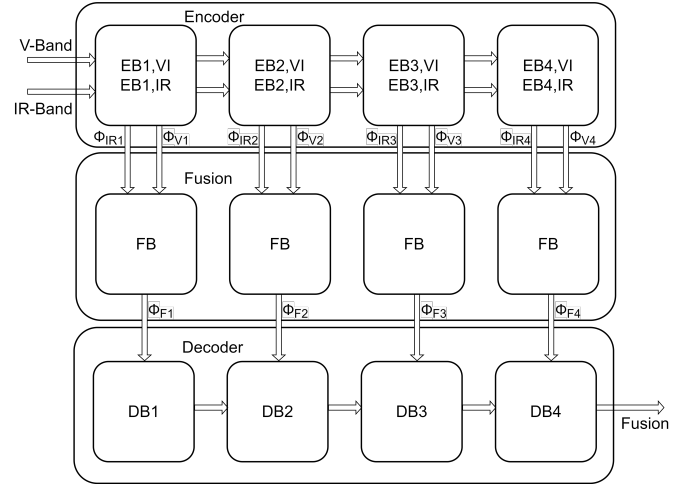


Fig. 2: FuseFormer Block Diagram

input images. Subsequently, the feature fuser merges these extracted features into unified feature maps for each level. These consolidated features play a crucial role in the final image reconstruction, orchestrated by the image reconstructor.

The same idea may be used to theoretically explain the model architecture that we present in this article as seen in Figure 2. In terms of analogy, the feature extractor corresponds to an encoder, while the image reconstructor aligns with a decoder for modern DL architectures. Both the visible and IR-band images are fed into this encoder first. The encoder outputs multiscale features, denoted as ϕ_{Vi} and ϕ_{IRi} . These features are then fed into the proposed a feature fuser (the middle component in Figure 2), which leverages both Convolutional Neural Networks (CNNs) and transformers, to manage both local features and global contexts. In the following, we provide the architectural details and the strategies we use to separately train each of these components.

A. Autoencoder Training

Our approach involves a two-stage training process. In the initial stage, we concurrently train the encoder and the decoder in Figure 2, by training an autoencoder, originally derived from RFN-Nest [44] as illustrated in Figure 3. Subsequently, in the second stage, we train our fusion block, depicted in Figure 4, in conjunction with the previously trained encoder and the decoder.

The initial phase of the training process involves instructing the encoder network to capture multi-scale deep features. Concurrently, the decoder network is also trained to reconstruct the encoder output. The extracted multi-scale deep features (ϕ_{IRi} and ϕ_{Vi}) are fed into the decoder network to reconstruct the input image. As explained in detail in [44], leveraging short cross-layer connections ensures the utilization of the multi-scale deep features in the image reconstruction process.

While training the autoencoder, the loss function, denoted as L_{ae} , serves as the main criterion and is defined in [44] in the subsequent manner:

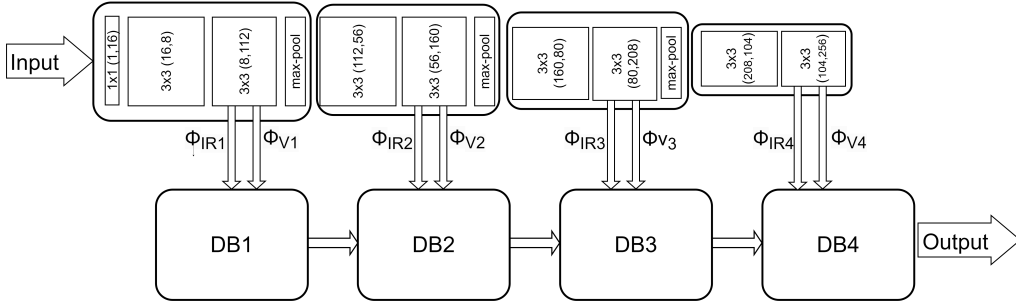


Fig. 3: The autoencoder architecture, derived from RFN-Nest [44]

$$L_{ae} = L_{pixel} + \alpha L_{SSIM} \quad (1)$$

The terms L_{pixel} and L_{SSIM} refer to the pixel loss and the structural similarity (SSIM) loss, respectively, computed between the input and output images. The parameter α represents the trade-off parameter governing the balance between the contributions of L_{pixel} and L_{SSIM} meanwhile also it handles the order of magnitude difference in the overall loss function in Eq 1.

$$L_{pixel} = ||I_{output} - I_{input}||_F^2 \quad (2)$$

L_{pixel} is defined in Eq 2. where $||\cdot||_F$ denotes Frobenius norm. L_{pixel} ensures that the reconstructed image closely resembles the original input image at the individual pixel level, imposing a constraint on the fidelity of pixel-wise information in the reconstruction process. This constraint helps to maintain fine-grained details and accuracy in the reconstructed image, ensuring that it retains the essential characteristics of the input image at a granular level.

The second term in Eq 1 is the SSIM loss L_{SSIM} and is defined as:

$$L_{SSIM} = 1 - SSIM(I_{output}, I_{input}) \quad (3)$$

where $SSIM(\cdot)$ is the structural similarity measure [31] which quantifies a measure of similarity between the two images. L_{SSIM} . SSIM is a widely used metric for evaluating the similarity between two images. It aims to capture not only the pixel-wise differences but also the structural information and perceptual quality of the images. ($SSIM$) metric outputs values within the range of -1 to 1. The output value 1 for the $SSIM(\cdot, \cdot)$ function denotes perfect similarity, indicating that the images share same characteristics in terms of luminance, contrast, and structure. Conversely, a value close to -1 signifies a substantial dissimilarity between the images. Notably, the $SSIM(\cdot, \cdot)$ index demonstrates a strong correlation with human perception of image quality, making it widely employed in diverse image processing and computer vision applications [31].

The $SSIM$ constrains its output to the range of $[-1, 1]$, which consequently bounds the L_{SSIM} loss function (as defined in Eq. 3) to the interval $[0, 2]$. In this context, lower

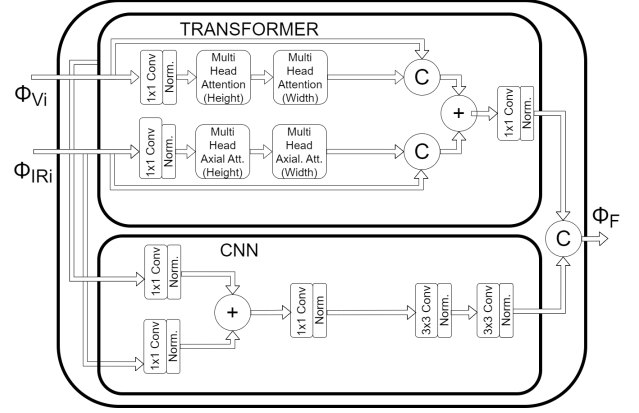


Fig. 4: The Fusion Block

values of L_{SSIM} indicate better performance with respect to $SSIM$. In contrast, the L_{pixel} loss is unbounded. To balance the impact of both L_{pixel} and L_{SSIM} during training, the trade-off parameter α in Eq. 1 governs their relative magnitudes.

B. Fusion Block Training

After successfully extracting multi-scale multi-level features in first stage, the aim in the second stage training is to merge the features from the two input images. In this stage, the RGB and IR features extracted from the encoder are merged into a single multi-scale feature map with fusion block as depicted in Figure 4. This fusion process aims at combining diverse features from different bands. The fusion block is characterised by its dual-branch design, which consists of a spatial branch and a transformer branch. The spatial branch consisting of CNN blocks facilitates fusion through the merge of local features. CNNs provide regional spatial coding but they lack the ability to model the global context and long spatial dependencies. To overcome this limitation, transformer-based models are included in the Fusion Block, which utilize axial attention mechanism to effectively model the global context. As can be seen in Figure 4, for each visible and infrared band image, two multi-head axial attention blocks are utilized, separately for each image dimension. The feature output of the attention blocks is concatenated with the original

encoder features (i.e., ϕ_{IRi} and ϕ_{Vi}) before being convolved for the final ϕ_{Fi} fused image construction.

Following the fusion, the resulting multi-scale feature maps, ϕ_{Fi} , are subsequently decoded, leading to the reconstruction of the original image. Decoding phase reconstructs an image that encapsulates the combined information from both bands. Hence, the reconstructed image, though visually similar to the input images, carries a richer set of features.

C. Fusion Loss

In the process of designing the loss function, contemporary studies persist with the identical loss formulation as presented in Eq. 1. This loss function incorporates a single input image, typically the visible band image, along with the output fused image. By neglecting the unused input image, typically the *infrared band image*, there arises a risk of overfitting towards the utilized input image. We can examine the edge loss circumstances in order to better visualize this phenomenon:

- $L_{pixel} = 0$ if and only if the input and output image is identical.
- $L_{ssim} = 0$ if and only if the input and output image is identical by definition of $SSIM(\cdot, \cdot)$.

A bias toward the SSIM and consequently the visible band picture is unavoidably created when the loss function is built as a combination of the two above. To overcome this, we propose a unique loss function. Namely, the fusion loss function L_{fuse} , similarly to L_{ae} , can be formulated as in Eq 4:

$$L_{fuse} = L_{feature} + \alpha L_{ssim} \quad (4)$$

This fusion loss function aims to balance the contribution from pixel-level losses, denoted as $L_{feature}$, and structural similarity losses, L_{ssim} , modulated by a trade-off factor, α which handles the difference of order of magnitude for losses. While defining these two loss components, the following constraints need to be considered:

- 1) The fused image should have a higher resemblance to the visual band image while maintaining the global context from the infrared band image almost identical to the visual band image. As a result, L_{ssim} must be computed for both input visual and infrared band images, ideally but not necessarily favoring the visual band image.
- 2) The pixel values of the fused image should closely match the visual band image due to its compatibility with human vision. Hence, $L_{feature}$ must be calculated on both input visual and infrared band images.

Then, The updated SSIM loss, L_{ssim} , is defined as:

$$L_{ssim} = [1 - SSIM(I_f, I_v)]^2 + [1 - SSIM(I_f, I_i)]^2 \quad (5)$$

The updated L_{ssim} is capable of measuring the similarity of the fused image to both visual and infrared images, and is limited to the interval $(0, 8]$.

The updated pixel-wise loss $L_{feature}$ can be formulated as:

$$L_{feature} = \sum_{m=1}^M \omega^m \|\phi_f^m - (\omega_{vi}\phi_{vi}^m + \omega_{ir}\phi_{ir}^m)\|_F^2 \quad (6)$$

Here, M refers to the number of scales for deep feature extraction, while f , vi , and ir denote the fused image, the input visual band image, and the input infrared band image respectively. ω^m , ω_{vi} , and ω_{ir} represent trade-off parameters employed to harmonize the magnitudes of the losses. ϕ_f^m corresponds to the feature maps of an image scale m , as depicted in Figure 2.

This loss function restricts the fused deep features to preserve significant structures, thereby enriching the fused feature space with more conspicuous features and preserving detailed information.

The model training process involved the utilization of three distinct datasets: MS-COCO [45] for autoencoder training in first stage, RoadScene [46] for integration of fusion strategies in second stage, and TNO [47] for comparative analysis. To ensure an unbiased and comprehensive evaluation, a partitioning approach was employed, dividing each dataset into **80%**, **10%**, and **10%** subsets, respectively assigned to the training, testing, and validation sets.

The hardware setup comprised an **NVIDIA RTX 3060Ti** featuring 16GB of memory, combined with an **Intel i9** 10th generation CPU. Throughout the model comparison, the assessment primarily relied on the following metrics: Entropy (En) [48], Sum of the Correlations of Differences (SCD) [49], Mutual Information (MI) [50], and Structural Similarity Index Metric (SSIM) [31].

IV. EXPERIMENTS AND RESULTS

TABLE I: Quantitative comparison of the loss Functions

Method	Entropy [48]↑	SCD [49]↓	MI [50]↑	SSIM [31]↑
L_{fuse}	4.536	5.433	1.591	0.884
L_{ae}	4.559	6.466	0.552	0.879
RFN-Nest	4.729	7.062	0.602	0.541

Our initial set of experiments focuses on analyzing the impact of the updated loss function. We primarily train the proposed FuseFormer architecture separately using the loss functions L_{fuse} and L_{ae} . In addition, the results of the autoencoder architecture (without the fusion block) and using the conventional loss function L_{ae} , are reported from the RFN-Nest [44] original paper. In Table I, comparative results with different evaluation metrics, including Entropy [48], SCD [49], MI [50], and SSIM [31] are provided. The proposed FuseFormer architecture, trained using the L_{fuse} loss function performs the best in 3 of the 4 evaluation metrics, including the original SSIM metric, although not only the visible band image is utilized for the updated SSIM loss metric L_{ssim} . When we observe samples as seen in Figure 5, we can see that redefinition of L_{ssim} not only enhances quantitative results but also improves qualitative outcomes. For instance, in the leftmost image, the person laying on the ground shows better visibility in Figure 5c, when compared to Figure 5d.

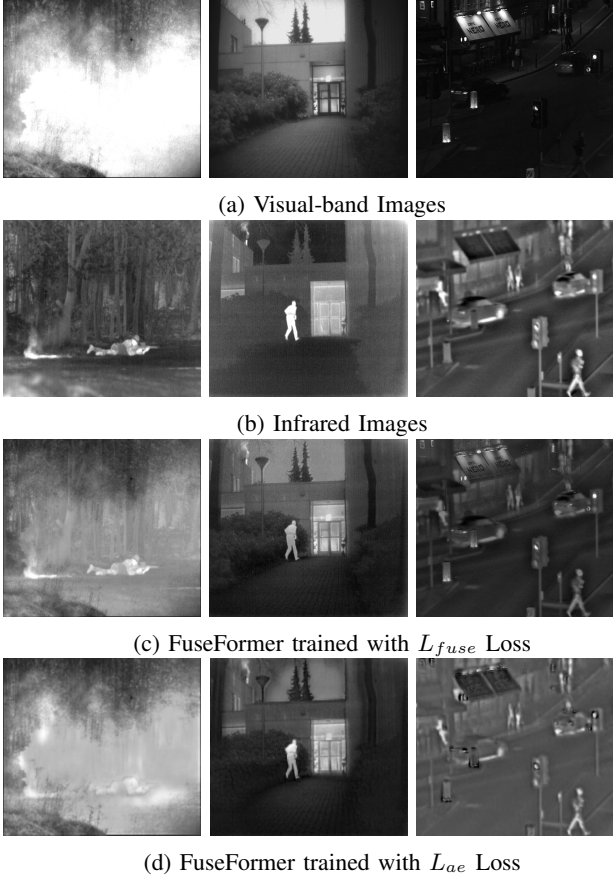


Fig. 5: Visual comparison of the loss functions

In our second set of experiments, we benchmark the FuseFormer architecture trained with the proposed L_{fuse} loss function, against the state-of-the-art (SoTa) fusion methods from the literature. For this comparison, we utilize SwinFusion [27], M3FD [51], RFN-Nest [44] and DenseFuse [8] models. In Table II, quantitative results are provided. In parallel with the result of Table I, FuseFormer performs the best for the same three evaluation metrics, including the original SSIM. In Figure 6, a qualitative comparison is also depicted.

For the purpose of doing a visual analysis for night vision settings, we carefully select a group of images from the TNO dataset that primarily show scenes taken in low light. These images are the two right-most columns in Figure 6. In this figure, the original visible-band and infrared images, our results, and the result of the selected SoTa methods are provided. Lighting at night creates a global effect in these

TABLE II: Quantitative comparison against the SoTa methods.

Method	Entr. [48]↑	SCD [49]↓	MI [50]↑	SSIM [31]↑
FuseFormer	4.536	5.433	1.591	0.884
SwinFusion	4.605	6.760	0.804	0.690
M3FD	4.625	6.858	0.742	0.659
DenseFuse	4.724	6.455	0.853	0.588
RFN-Nest	4.729	7.062	0.602	0.541

images, hence, they effectively demonstrate the long-range dependencies (i.e. global context) present in these scenarios. We observe that FuseFormer outperforms or is comparable with the SoTa approaches, in all scenarios.

TABLE III: Model tuning Experiments: Transformer Layers

Exp.	Entropy [48]↑	SCD [49]↓	MI [50]↑	SSIM [31]↑
T_{12}	4.533	6.152	1.346	0.846
T_{10}	4.535	6.335	1.232	0.824
T_8	4.587	6.657	0.874	0.719

TABLE IV: Model tuning Experiments: Batch Size

Exp.	Entropy [48]↑	SCD [49]↓	MI [50]↑	SSIM [31]↑
B_4	4.542	6.478	1.130	0.746
B_2	4.587	6.657	0.874	0.719

TABLE V: Model tuning Experiments: Learning Rate

Exp.	Entropy [48]↑	SCD [49]↓	MI [50]↑	SSIM [31]↑
LR_{1e-6}	4.553	6.551	1.032	0.774
LR_{1e-5}	4.570	6.603	0.948	0.747
LR_{1e-4}	4.587	6.657	0.874	0.719

TABLE VI: Model tuning Experiments: Improvement Rate

Criteria	Initial V	Optimized V	Improvement (%)
Learning Rate	1×10^{-4}	1×10^{-6}	7.64%
Batch Size	2	4	3.8%
Transformer Layers	8	12	18.15%

A. Model Tuning Experiments

In the last round of our experiments, we investigate the impact of adjusting certain hyperparameters to fine-tune our model for improved functionality. First, we provide the quantitative performance of the models with 8, 10, and 12 transformer layers in Table III to assess the effect of increasing the number of transformer layers. It is seen that as the capacity of the model is increased there is still room for improvement. However, this improvement comes with a huge computation demand and increases the convergence time quadratically. Table IV shows that, changing the batch size does not affect the model performance significantly, which is expected. According to Table V, changing the learning rate adaptively during training, improves quantitative results. Our experience with the model also demonstrates that convergence is improved by beginning with a greater learning rate value and gradually lowering it as training progresses. We finally describe the improvements achieved by adjusting these three hyperparameters in Table VI. A key takeaway from the tuning trials is that more processing power for training can enhance the quantitative results even more.

V. CONCLUSION

In this paper, we proposed the ‘‘FuseFormer’’ architecture, which is a transformer+CNN-based visible-infrared band image fusion network. Our proposed dual-branch fusion strategy utilizes a CNN and a transformer branch, which fuse local and

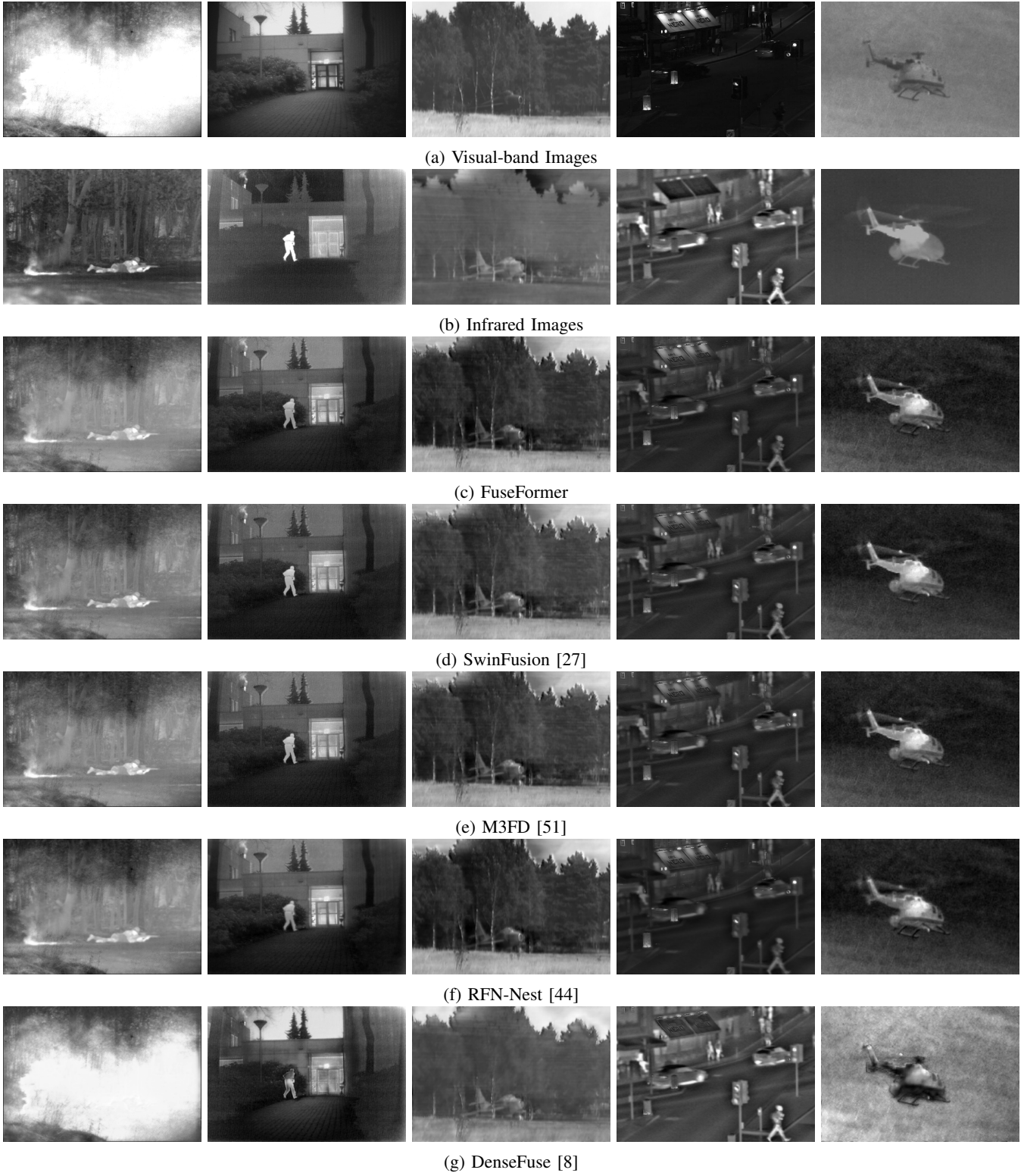


Fig. 6: Visual Comparison of the SoTa methods for general conditions. The two right-most scenarios present low-light conditions.

global features. The proposed method is evaluated on fusion benchmark datasets where we achieve competitive results compared to the existing fusion methods. We also develop a novel fusion strategy with a novel loss function that contributes from both input (i.e. visible-band and infrared) images and takes global context into account. We even achieve better quantitative results using the original SSIM metric, despite updating this metric in the loss function to benefit from both the visible-band and the infrared image.

Image fusion presents a fundamental challenge directed towards accommodating human observers rather than algorithms, requiring additional investigation across diverse spectral bands and scenarios. However, the fusion process can also be used to improve downstream activities such as feature fusion. With the increasing integration of vision transformers, we believe that there's optimism for achieving a universal fusion solution independent of the input bands and scenarios.

REFERENCES

- [1] Z. Liu, E. Blasch, Z. Xue, J. Zhao, R. Laganiere, and W. Wu, "Objective assessment of multiresolution image fusion algorithms for context enhancement in night vision: a comparative study," *IEEE transactions on pattern analysis and machine intelligence*, vol. 34, no. 1, pp. 94–109, 2011.
- [2] S. Chaudhari, G. Deshmukh, S. Gokhale, R. Kadu, S. Jahirabadkar, and R. Aditya, "A survey of visible and infrared image fusion methodologies," in *Inventive Communication and Computational Technologies* (G. Ranganathan, G. A. Papakostas, and Á. Rocha, eds.), (Singapore), pp. 1057–1070, Springer Nature Singapore, 2023.
- [3] M. Belgiu and A. Stein, "Spatiotemporal image fusion in remote sensing," *Remote Sensing*, vol. 11, no. 7, 2019.
- [4] H. Hermessi, O. Murali, and E. Zagrouba, "Multimodal medical image fusion review: Theoretical background and recent advances," *Signal Processing*, vol. 183, p. 108036, 2021.
- [5] A. Toet, L. J. Van Ruyven, and J. M. Valetton, "Merging thermal and visual images by a contrast pyramid," *Optical engineering*, vol. 28, no. 7, pp. 789–792, 1989.
- [6] K. Song, Y. Zhao, L. Huang, Y. Yan, and Q. Meng, "Rgb-t image analysis technology and application: A survey," *Engineering Applications of Artificial Intelligence*, vol. 120, p. 105919, 2023.
- [7] Y. Zhang, Y. Liu, P. Sun, H. Yan, X. Zhao, and L. Zhang, "Ifcnn: A general image fusion framework based on convolutional neural network," *Information Fusion*, vol. 54, pp. 99–118, 2020.
- [8] H. Li, X.-j. Wu, and T. S. Durrani, "Infrared and visible image fusion with resnet and zero-phase component analysis," *Infrared Physics & Technology*, vol. 102, p. 103039, 2019.
- [9] A. Raza, H. Huo, and T. Fang, "Pfaf-net: Pyramid feature network for multimodal fusion," *IEEE Sensors Letters*, vol. 4, no. 12, pp. 1–4, 2020.
- [10] Z. Zhao, S. Xu, J. Zhang, C. Liang, C. Zhang, and J. Liu, "Efficient and model-based infrared and visible image fusion via algorithm unrolling," *IEEE Transactions on Circuits and Systems for Video Technology*, vol. 32, no. 3, pp. 1186–1196, 2021.
- [11] Y. Fu and X. Wu, "A dual-branch network for infrared and visible image fusion," in *2020 25th International Conference on Pattern Recognition (ICPR)*, (Los Alamitos, CA, USA), pp. 10675–10680, IEEE Computer Society, jan 2021.
- [12] L. Jian, X. Yang, Z. Liu, G. Jeon, M. Gao, and D. Chisholm, "Sedrfuse: A symmetric encoder–decoder with residual block network for infrared and visible image fusion," *IEEE Transactions on Instrumentation and Measurement*, vol. 70, pp. 1–15, 2020.
- [13] Z. Wang, Y. Wu, J. Wang, J. Xu, and W. Shao, "Res2fusion: Infrared and visible image fusion based on dense res2net and double nonlocal attention models," *IEEE Transactions on Instrumentation and Measurement*, vol. 71, pp. 1–12, 2022.
- [14] I. Goodfellow, J. Pouget-Abadie, M. Mirza, B. Xu, D. Warde-Farley, S. Ozair, A. Courville, and Y. Bengio, "Generative adversarial networks," in *Advances in neural information processing systems*, pp. 2672–2680, 2014.
- [15] J. Ma, W. Yu, P. Liang, C. Li, and J. Jiang, "Fusiongan: A generative adversarial network for infrared and visible image fusion," *Information fusion*, vol. 48, pp. 11–26, 2019.
- [16] J. Xu, X. Shi, S. Qin, K. Lu, H. Wang, and J. Ma, "Lbp-began: A generative adversarial network architecture for infrared and visible image fusion," *Infrared Physics & Technology*, vol. 104, p. 103144, 2020.
- [17] D. Xu, Y. Wang, S. Xu, K. Zhu, N. Zhang, and X. Zhang, "Infrared and visible image fusion with a generative adversarial network and a residual network," *Applied Sciences*, vol. 10, no. 2, p. 554, 2020.
- [18] Y. Fu, X.-J. Wu, and T. Durrani, "Image fusion based on generative adversarial network consistent with perception," *Information Fusion*, vol. 72, pp. 110–125, 2021.
- [19] J. Ma, H. Zhang, Z. Shao, P. Liang, and H. Xu, "Ganmcc: A generative adversarial network with multiclassification constraints for infrared and visible image fusion," *IEEE Transactions on Instrumentation and Measurement*, vol. 70, pp. 1–14, 2020.
- [20] J. Liu, X. Fan, J. Jiang, R. Liu, and Z. Luo, "Learning a deep multi-scale feature ensemble and an edge-attention guidance for image fusion," *IEEE Transactions on Circuits and Systems for Video Technology*, vol. 32, no. 1, pp. 105–119, 2021.
- [21] B. Liao, Y. Du, and X. Yin, "Fusion of infrared-visible images in ue-iot for fault point detection based on gan," *IEEE Access*, vol. 8, pp. 79754–79763, 2020.
- [22] A. Dosovitskiy, L. Beyer, A. Kolesnikov, D. Weissenborn, X. Zhai, T. Unterthiner, M. Dehghani, M. Minderer, G. Heigold, S. Gelly, *et al.*, "An image is worth 16x16 words: Transformers for image recognition at scale," *arXiv preprint arXiv:2010.11929*, 2020.
- [23] Z. Liu, Y. Lin, Y. Cao, H. Hu, Y. Wei, Z. Zhang, S. Lin, and B. Guo, "Swin transformer: Hierarchical vision transformer using shifted windows," in *Proceedings of the IEEE/CVF international conference on computer vision*, pp. 10012–10022, 2021.
- [24] X. Liu, H. Gao, Q. Miao, Y. Xi, Y. Ai, and D. Gao, "Mfst: Multi-modal feature self-adaptive transformer for infrared and visible image fusion," *Remote Sensing*, vol. 14, no. 13, p. 3233, 2022.
- [25] V. Vs, J. M. J. Valanarasu, P. Oza, and V. M. Patel, "Image fusion transformer," in *2022 IEEE International Conference on Image Processing (ICIP)*, pp. 3566–3570, IEEE, 2022.
- [26] Y. Fu, T. Xu, X. Wu, and J. Kittler, "Ppt fusion: Pyramid patch transformer for a case study in image fusion," *arXiv preprint arXiv:2107.13967*, 2021.
- [27] J. Ma, L. Tang, F. Fan, J. Huang, X. Mei, and Y. Ma, "Swinfusion: Cross-domain long-range learning for general image fusion via swin transformer," *IEEE/CAA Journal of Automatica Sinica*, vol. 9, no. 7, pp. 1200–1217, 2022.
- [28] L. Qu, S. Liu, M. Wang, S. Li, S. Yin, Q. Qiao, and Z. Song, "Transfuse: A unified transformer-based image fusion framework using self-supervised learning," *arXiv preprint arXiv:2201.07451*, 2022.
- [29] H. Zhao and R. Nie, "Dndt: Infrared and visible image fusion via densenet and dual-transformer," in *2021 International Conference on Information Technology and Biomedical Engineering (ICITBE)*, pp. 71–75, IEEE, 2021.
- [30] X. Yang, H. Huo, R. Wang, C. Li, X. Liu, and J. Li, "Dglt-fusion: A decoupled global–local infrared and visible image fusion transformer," *Infrared Physics & Technology*, vol. 128, p. 104522, 2023.
- [31] K. Ma, K. Zeng, and Z. Wang, "Perceptual quality assessment for multi-exposure image fusion," *IEEE Transactions on Image Processing*, vol. 24, no. 11, pp. 3345–3356, 2015.
- [32] P. Jagalingam and A. V. Hegde, "A review of quality metrics for fused image," *Aquatic Procedia*, vol. 4, pp. 133–142, 2015. International Conference On Water Resources, Coastal And Ocean Engineering (ICWRCOE'15).
- [33] Y. Bin, Y. Chao, and H. Guoyu, "Efficient image fusion with approximate sparse representation," *International Journal of Wavelets, Multiresolution and Information Processing*, vol. 14, no. 04, p. 1650024, 2016.
- [34] Q. Zhang, Y. Fu, H. Li, and J. Zou, "Dictionary learning method for joint sparse representation-based image fusion," *Optical Engineering*, vol. 52, no. 5, pp. 057006–057006, 2013.
- [35] H.-M. Hu, J. Wu, B. Li, Q. Guo, and J. Zheng, "An adaptive fusion algorithm for visible and infrared videos based on entropy and the cumulative distribution of gray levels," *IEEE Transactions on Multimedia*, vol. 19, no. 12, pp. 2706–2719, 2017.

- [36] K. He, D. Zhou, X. Zhang, R. Nie, Q. Wang, and X. Jin, "Infrared and visible image fusion based on target extraction in the nonsubsampling contourlet transform domain," *Journal of Applied Remote Sensing*, vol. 11, no. 1, pp. 015011–015011, 2017.
- [37] G. Liu, Z. Lin, S. Yan, J. Sun, Y. Yu, and Y. Ma, "Robust recovery of subspace structures by low-rank representation," *IEEE transactions on pattern analysis and machine intelligence*, vol. 35, no. 1, pp. 171–184, 2012.
- [38] H. Xu, J. Ma, J. Jiang, X. Guo, and H. Ling, "U2fusion: A unified unsupervised image fusion network," *IEEE Transactions on Pattern Analysis and Machine Intelligence*, vol. 44, no. 1, pp. 502–518, 2022.
- [39] Y. Liu, X. Chen, J. Cheng, H. Peng, and Z. Wang, "Infrared and visible image fusion with convolutional neural networks," *International Journal of Wavelets, Multiresolution and Information Processing*, vol. 16, no. 03, p. 1850018, 2018.
- [40] H. Xu, P. Liang, W. Yu, J. Jiang, and J. Ma, "Learning a generative model for fusing infrared and visible images via conditional generative adversarial network with dual discriminators," in *IJCAI*, pp. 3954–3960, 2019.
- [41] Z. Wang, Y. Chen, W. Shao, H. Li, and L. Zhang, "Swinfuse: A residual swin transformer fusion network for infrared and visible images," *IEEE Transactions on Instrumentation and Measurement*, vol. 71, pp. 1–12, 2022.
- [42] X. Zhang and Y. Demiris, "Visible and infrared image fusion using deep learning," *IEEE Transactions on Pattern Analysis and Machine Intelligence*, vol. 45, no. 8, pp. 10535–10554, 2023.
- [43] K. I. Danaci and E. Akagunduz, "A survey on infrared image & video sets," *Multimedia Tools and Applications*, vol. 83, pp. 16485–16523, Feb 2024.
- [44] H. Li, X.-J. Wu, and J. Kittler, "Rfn-nest: An end-to-end residual fusion network for infrared and visible images," *Information Fusion*, vol. 73, pp. 72–86, 2021.
- [45] T.-Y. Lin, M. Maire, S. Belongie, J. Hays, P. Perona, D. Ramanan, P. Dollár, and C. L. Zitnick, "Microsoft coco: Common objects in context," in *Computer Vision—ECCV 2014: 13th European Conference, Zurich, Switzerland, September 6–12, 2014, Proceedings, Part V 13*, pp. 740–755, Springer, 2014.
- [46] H. Xu, J. Ma, Z. Le, J. Jiang, and X. Guo, "FusionDn: A unified densely connected network for image fusion," in *Proceedings of the AAAI conference on artificial intelligence*, vol. 34, pp. 12484–12491, 2020.
- [47] A. Toet *et al.*, "Tno image fusion dataset; https://figshare.com/articles/TN_Image_Fusion_Dataset/1008029, 2014.
- [48] J. W. Roberts, J. A. Van Aardt, and F. B. Ahmed, "Assessment of image fusion procedures using entropy, image quality, and multispectral classification," *Journal of Applied Remote Sensing*, vol. 2, no. 1, p. 023522, 2008.
- [49] V. Aslantas and E. Bendes, "A new image quality metric for image fusion: The sum of the correlations of differences," *Aeu-international Journal of electronics and communications*, vol. 69, no. 12, pp. 1890–1896, 2015.
- [50] G. Qu, D. Zhang, and P. Yan, "Information measure for performance of image fusion," *Electronics letters*, vol. 38, no. 7, p. 1, 2002.
- [51] J. Liu, X. Fan, Z. Huang, G. Wu, R. Liu, W. Zhong, and Z. Luo, "Target-aware dual adversarial learning and a multi-scenario multi-modality benchmark to fuse infrared and visible for object detection," in *Proceedings of the IEEE/CVF Conference on Computer Vision and Pattern Recognition*, pp. 5802–5811, 2022.